The periodically extended stiffness nonlinear energy sink

Kevin Dekemele[a,*], Giuseppe Habib[b], Mia Loccufier[a]

[a] *Ghent University, Department of Electromechanical, Systems and Metal Engineering, Tech Lane Ghent Science Park - Campus A 125, 9052, Ghent, Belgium*
[b] *Budapest University of Technology and Economics, Department of Applied Mechanics, MTA-BME Lendület Machine Tool Vibration Research Group, Műegyetem rkp. 5., H-1111,Budapest, Hungary*

Abstract

Conventional nonlinear energy sinks (NES) are considered to be a more robust alternative to linear vibration absorbers such as the tuned-mass-damper (TMD). While the conventional NES has a larger efficient frequency bandwidth than the TMD, it is only really efficient for a small energy range. This implies a deterioration of the NES's mitigation properties if the primary system's amplitude varies. To overcome this issue, other researchers resort to increasing the complexity of the NES by adding degrees-of-freedom. Here, another line of thought is presented, by proposing an unconventional stiffness characteristic. To increase the energy bandwidth the NES in this paper features a non-smooth, periodically extended stiffness characteristic. This NES is attached to an uncertain primary system and its performance is compared with that of the conventional NES and of the TMD by deriving the slow invariant manifolds (SIMs) in transient 1:1 resonance. The SIMs are curves that relate the vibration amplitudes of the primary system and the NES, and serve as an easy and computationally efficient tool to analyze performance. The research in this paper will prove that the newly proposed NES can be both robust regarding energy and frequency uncertainty, by considering the novel periodically extended stiffness characteristic.

Keywords: Nonlinear Energy Sink, Passive Vibration Control, Dynamic Vibration Absorber, Tuned Mass Damper, Periodic Stiffness

1. Introduction

The linear tuned-mass-damper (TMD) vibration absorber has been investigated and implemented as a means to mitigate vibrations of a mechanical structure, since its inception in a 1909 [1] patent. It was further improved in a 1928

*Corresponding Author
Email address: kevin.dekemele@ugent.be (Kevin Dekemele)

textbook [2]. These are light-weight auxiliary devices, consisting of a mass that is spring-connected to the vibrating system. An efficient TMD is designed by approximately matching the TMD's natural frequency with the vibration frequency of the mechanical structure. This requires accurate knowledge of the vibratory properties of the primary system. If the frequency of vibration shifts because of uncertainties or modifications to the primary system, the TMD performance deteriorates. Therefore, researchers have proposed the nonlinear energy sink (NES), a light-weight device consisting of a mass that is nonlinearly connected to the primary system [3, 4, 5, 6, 7]. The nonlinearity gives the NES a variable natural frequency and as such a 'self-tuning' property [8]. This means that an NES can efficiently mitigate vibrations over a wide frequency bandwidth. As such, it can efficiently deal with shifting vibration frequencies and vibrations that consist of several modes [9, 10, 11]. Although the NES has shown to have attractive properties with regards to frequency bandwidth, its main limitation lies in its narrow energy bandwidth. This means that it is only efficient for a limited range of vibration amplitude levels. In the aforementioned investigations of the NES, the connecting stiffness is almost exclusively a hardening cubic stiffness characteristic. However, as shown later in this study, this choice of characteristic limits the NES performance.

To overcome the downsides of the conventional NES, literature follows two lines of thought. Either the complexity of the NES is increased by adding degrees-of-freedom (DOF)/additional mechanisms, or other stiffness characteristics are proposed. In the first line of thought, works have investigated 2DOF series NESs [12], a chain of NESs [13], or a conventional NES featuring an additional pendulum [14]. A complex mechanism was added to a conventional NES in [15] where two masses oscillated with a constant frequency on top of the NES. This increased dimensionality of the NES complicates the analysis of the global dynamics.
In the other line of thought, researchers investigate slight variations or additions to the conventional NES stiffness characteristics. In [16, 17] an NES possessing bistability properties was investigated. Other polynomial stiffnesses were featured in [18, 10]. Recently, an interesting characteristic was proposed in [19]. It consists of two piecewise cubic characteristics. The transition from the first to the second characteristics causes a non-smooth descent before hardening again. The performance of NESs with slightly different characteristics are only slightly better than the conventional NESs. However, the proposed characteristics are often based on mechanisms that mimic these stiffnesses. The conventional cubic stiffness can be attained with transversely loaded strings [20], the bistable stiffness with a pre-stressed beam or through permanent magnets [21] and the two piecewise characteristics with a magnet assembly [19].

Other works have proposed a periodic stiffness function with rotational NES variants. In [22], authors proposed the so-called rotational NES, consisting of

a rotating eccentric mass, attached to the primary system to be controlled. In spite of its simple and compact design, several studies [22, 23, 24, 25, 26, 27, 28] proved the good and broadband performance of the rotational NES, however, this is achieved only if rotational motion is triggered [22, 25, 26]. Furthermore, this kind of NES is very sensitive to its damping [26] and initial conditions [22]. Its effectiveness was evaluated analytically [22, 23, 25], numerically and experimentally [22, 24, 26, 27], against impulsive excitations [22, 23, 24, 25, 26, 27] and for vortex-induced vibration mitigation [28].

In this work, the second line of thought will be followed but the authors will shy away from the slight variations on the cubic stiffness by proposing an unconventional stiffness characteristic, a periodically-extended polynomial stiffness. For small displacements, this characteristic is a cubic polynomial stiffness, but for larger displacements descents to then again harden as a cubic polynomial. This descent and hardening is periodic. The authors are motivated by recent works that propose and implement simple devices that can tailor-make any nonlinear stiffness characteristic. In [29, 30], this tailor-made stiffness is attained by compressing a spring along an arbitrarily shaped force-profile. The desired stiffness was obtained by 3D-printing or CNC-machining this profile with a shape that approximately corresponds to the elastic potential energy of the proposed stiffness characteristic. Others have proposed a topology optimized 3D-printed beam, but have only realized slightly hardening spring characteristics [31].
To analyze the performance of the proposed NES and compare it to the conventional NES in a computationally efficient manner, the slow invariant manifold (SIM) is exploited. The SIM is a static expression that relates the primary system's vibration amplitude to the NES's amplitude. It has been used to find conditions for efficient energy transfer and can be directly related to the speed and duration of the energy transfer under transient conditions [32, 10]. The research in this paper will prove that an efficient and robust (in both frequency and energy) single DOF NES can be obtained by considering an unconventional stiffness.
To show this, the paper is structured as follows. Section 2 presents the novel NES and the primary system. The considered primary system has an uncertainty on its stiffness and thus on its natural frequency. Then, in section 3, the SIM of the novel NES is derived in function of the uncertainty. It is compared to the SIMs of the conventional NES and TMD. Stability and dynamics along the SIM is computed. Numerical simulations with the novel NES will confirm that the SIM is a good predictor of performance. Section 4 investigates the influence of the primary system's uncertainty. It will be shown that the novel NES presented here is superior in frequency and energy bandwidth under certain conditions, compared to the conventional NES and TMD. Finally, the conclusion is presented.

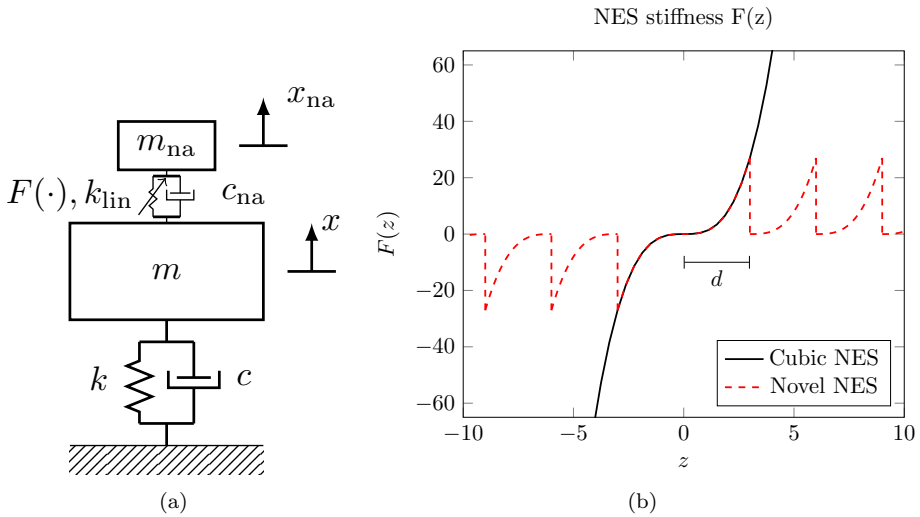

Figure 1: The primary system with an NES (a) and the connecting stiffness characteristic of conventional NESs and of the proposed periodically extended NES (b).

2. Model description and novel stiffness

The studied compound system constitutes the primary system and the NES and is shown in Figure 1a where m, c, and k are the primary system's mass, damping and stiffness and where m_{na}, c_{na} and $F(\cdot)$ are the NES's mass, damping and nonlinear connecting stiffness characteristic, respectively. The stiffness k_{lin} is a linear connecting stiffness, only present if a TMD is considered as a vibration absorber. Finally, x and x_{na} indicate the translational displacement of the primary system and of the NES, respectively. The system's dynamics are described by the following set of differential equations:

$$\begin{aligned} m\ddot{x} + c\dot{x} + kx + c_{\mathrm{na}}(\dot{x} - \dot{x}_{\mathrm{na}}) + k_{\mathrm{lin}}(x - x_{\mathrm{na}}) + k_{\mathrm{na}}F(x - x_{\mathrm{na}}) = 0 \\ m_{\mathrm{na}}\ddot{x}_{\mathrm{na}} + c_{\mathrm{na}}(\dot{x}_{\mathrm{na}} - \dot{x}) + k_{\mathrm{lin}}(x_{\mathrm{na}} - x) + k_{\mathrm{na}}F(x_{\mathrm{na}} - x) = 0 \end{aligned} \tag{1}$$

where k_{na} is the proportionality factor of connecting nonlinear stiffness. When the absorber is a NES, then $k_{\mathrm{lin}} = 0$, if it is a TMD, $k_{\mathrm{na}} = 0$ and finally if it is a simple dynamic viscous damper, also called the Lancaster damper, then both $k_{\mathrm{lin}} = 0$ and $k_{\mathrm{na}} = 0$. The primary system's stiffness k consists of an assumed stiffness k_{a} (where a stands for assumed) and an unknown stiffness variation k_{u} (where u stands for unknown), $k = k_{\mathrm{a}} + k_{\mathrm{u}}$. The assumed stiffness k_{a} is what the vibration absorber designer assumes when tuning the DVA, while k_{u} expresses a detuning unknown to the designer.

The nonlinear connecting stiffness $F(z)$, where $z = x_{\mathrm{na}} - x$, is a periodic extension

in $\mathbb{R}^+$ of z^3 defined in $0 < z < d$, and an extension in $\mathbb{R}^-$ of z^3 defined in $-d < z < 0$ to keep the function odd:

$$F(z) = \begin{cases} (z + i \cdot d)^3 & -(i+1)d \leq z < -id \text{ with } i \in \mathbb{N}^+ \\ z^3 & -d \leq z \leq d \\ (z - i \cdot d)^3 & id < z \leq (i+1)d \text{ with } i \in \mathbb{N}^+ \end{cases} \tag{2}$$

as such d is the periodicity of the extension. This stiffness is plotted in Figure 1b for $d = 3$. The concept for realizing such a NES is presented in Appendix A.

3. Slow invariant manifold: derivation, stability and numerical simulation

3.1. System

The equations in (1) are divided by the primary mass m:

$$\begin{aligned} &\ddot{x} + \epsilon\omega_0\xi\dot{x} + (1+\delta)\omega_0^2 x + \epsilon\ddot{x}_{\mathrm{na}} = 0 \\ &\epsilon\ddot{x}_{\mathrm{na}} + \epsilon\omega_0\xi_{\mathrm{na}}(\dot{x}_{\mathrm{na}} - \dot{x}) + \epsilon\omega_0^2\gamma F(x_{\mathrm{na}} - x) + \epsilon\omega_0^2\kappa(x_{\mathrm{na}} - x) = 0 \end{aligned} \tag{3}$$

with

$$\begin{aligned} \omega_0^2 = \frac{k_{\mathrm{a}}}{m} \quad \delta = \frac{k_{\mathrm{u}}}{k_{\mathrm{a}}} \quad \epsilon = \frac{m_{\mathrm{na}}}{m} \quad \xi_{\mathrm{na}} = \frac{c_{\mathrm{na}}}{m_{\mathrm{na}}\omega_0} \\ \xi = \frac{c}{\epsilon m \omega_0} \quad \gamma = \frac{k_{\mathrm{na}}}{m_{\mathrm{na}}\omega_0^2} \quad \kappa = \frac{k_{\mathrm{lin}}}{m_{na}\omega_0^2} \end{aligned} \tag{4}$$

The mass ratio is assumed small, $\epsilon \ll 1$. The unknown variation on the primary stiffness is expressed in δ. Under small ϵ, if perturbed, the compound system vibrates with a frequency approximately being $\omega_1 = \omega_0\sqrt{1+\delta}$. The frequency ω_0 is the frequency without uncertainty ($\delta = 0$). The dimensionless time is introduced, $\tau = \omega_1 t = \omega_0\sqrt{1+\delta}t$, the derivative to τ is denoted by $'$:

$$\begin{aligned} &x'' + \epsilon\frac{\xi}{\sqrt{1+\delta}}x' + x + \epsilon x''_{\mathrm{na}} = 0 \\ &\epsilon x''_{\mathrm{na}} + \epsilon\frac{\xi_{\mathrm{na}}}{\sqrt{1+\delta}}(x'_{\mathrm{na}} - x') + \epsilon\frac{\kappa}{1+\delta}(x_{\mathrm{na}} - x) + \epsilon\frac{\gamma}{1+\delta}F(x_{\mathrm{na}} - x) = 0 \end{aligned} \tag{5}$$

The differential equation (5) does not have closed-form solution so we search for a solution for the amplitudes of vibration through harmonic balancing.

3.2. Harmonic balancing

The relative absorber coordinate $z = x_{\mathrm{na}} - x$ is introduced. The dynamic variables x and z are assumed to vibrate with the same frequency, under a 1:1

resonance. The proposed solution is:

$$\begin{cases} x = \dfrac{Ae^{j\tau} - \bar{A}e^{-j\tau}}{2j} & z = \dfrac{Be^{j\tau} - \bar{B}e^{-j\tau}}{2j} \\ x' = \dfrac{Ae^{j\tau} + \bar{A}e^{-j\tau}}{2} & z' = \dfrac{Be^{j\tau} + \bar{B}e^{-j\tau}}{2} \end{cases} \tag{6}$$

where $A(\tau)$, $B(\tau) \in \mathbb{C}$. Deriving $A(\tau)e^{j\tau} = \dot{x}(\tau) + jx(\tau)$ and $B(\tau)e^{j\tau} = \dot{z}(\tau) + jz(\tau)$ yields after some steps:

$$\begin{aligned} x'' + x &= A'e^{j\tau} \\ z'' + z &= B'e^{j\tau} \end{aligned} \tag{7}$$

Inserting (6) and (7) into the absorber (second) equation of (5), we obtain:

$$\begin{aligned} B'e^{j\tau} + A'e^{j\tau} + \frac{\xi_{\text{na}}}{\sqrt{1+\delta}} \frac{Be^{j\tau} + \bar{B}e^{-j\tau}}{2} + \frac{\gamma}{1+\delta} F\left(\frac{Be^{j\tau} - \bar{B}e^{-j\tau}}{2j}\right) \\ + \frac{\kappa}{1+\delta}\left(\frac{Be^{j\tau} - \bar{B}e^{-j\tau}}{2j}\right) - \frac{Be^{j\tau} - \bar{B}e^{-j\tau}}{2j} - \frac{Ae^{j\tau} - \bar{A}e^{-j\tau}}{2j} = 0 \end{aligned} \tag{8}$$

Only the terms with frequency $e^{j\tau}$ are kept (harmonic balancing). For the term $F(z)$, this is determined from the first harmonic of its Fourier's series, $F(z) \approx f_1 e^{j\tau}$, a procedure explained in [33]:

$$f_1(B, \bar{B}) = \frac{1}{2\pi} \int_0^{2\pi} F\left(\frac{Be^{j\tau} - \bar{B}e^{-j\tau}}{2j}\right) e^{-i\tau} d\tau \tag{9}$$

For odd functions of $F(\frac{Be^{j\tau} - \bar{B}e^{-j\tau}}{2j})$ the integral (9) reduces to:

$$f_1(B, \bar{B}) = \frac{B}{2j} G(|B|) \tag{10}$$

where $G(|B|)$ is a real function [33]. The calculation of f_1 for the novel periodically extended NES is quite elaborate, and is therefore delegated to Appendix B. The harmonic balancing of (8) yields:

$$B'e^{j\tau} + A'e^{j\tau} + \frac{\xi_{\text{na}}}{\sqrt{1+\delta}} \frac{B}{2} + \frac{\gamma}{1+\delta} \frac{B}{2j} G(|B|) + \frac{\kappa}{1+\delta} \frac{B}{2j} - \frac{B}{2j} - \frac{A}{2j} = 0 \tag{11}$$

3.3. Slow invariant manifold

The slow invariant manifold (SIM) describes the slow dynamics of the system. In particular, it relates the amplitude of oscillation of the primary system to the absorber. Following the common approach utilized in the literature [33, 32,

34, 16, 10], the system is assumed in steady-state conditions. This approach is not rigorously correct since the system is in transient dynamics, and the only admissible steady-state solution is the trivial one. However, focusing on the slow dynamics of the system and temporarily neglecting damping terms in the slow dynamics, fictitious steady-state solutions can be found setting $A' = B' = 0$. A more elaborate two-timing scaling procedure section 3.4 will yield the same result. As illustrated below, this procedure enables us to obtain a function relating the amplitude of oscillation of the primary system to the one of the absorber. The complex amplitudes A and B are now written in their polar form $A = ae^{j\alpha}$ and $B = be^{j\beta}$. The equation (11) split up in real and complex parts are:

$$\begin{aligned} -a\sin(\alpha-\beta) =& \frac{\xi_{\text{na}}}{\sqrt{1+\delta}} b \\ -a\cos(\alpha-\beta) =& b - \frac{\kappa}{1+\delta} b - \frac{\gamma}{1+\delta} G(b) b \end{aligned} \tag{12}$$

Then, squaring and then adding the real and complex parts gives the slow invariant manifold (SIM) expression:

$$a^2 = \left(\frac{\xi_{\text{na}}^2}{1+\delta} + \left(1 - \frac{\kappa}{1+\delta} - \frac{\gamma}{1+\delta} G(b) \right)^2 \right) b^2 \tag{13}$$

When studying the NES, then $\kappa = 0$ and the SIM is :

$$a^2 = \left(\frac{\xi_{\text{na}}^2}{1+\delta} + \left(1 - \frac{\gamma}{1+\delta} G(b) \right)^2 \right) b^2 \tag{14}$$

In the case of the TMD ($\gamma = 0$ and $\kappa = 1$), the expression is reduced to:

$$a^2 = \left(\frac{\xi_{\text{na}}^2}{1+\delta} + \left(1 - \frac{1}{1+\delta} \right)^2 \right) b^2 \tag{15}$$

while for the Lancaster damper, the purely viscous damper with mass, ($\gamma = 0$ and $\kappa = 0$) to

$$a^2 = \left(\frac{\xi_{\text{na}}^2}{1+\delta} + 1 \right) b^2 \tag{16}$$

The SIM expresses the ratio between the primary mass's vibration amplitude a and the relative NES vibration amplitude b. Some SIMs are given in Figure 2 for $\xi_{\text{na}} = 0.15$ and $\delta = 0$. The solid blue line marks the SIM of the TMD, the blue dashed line indicates the SIM of Lancaster damper and the black curve represents the SIM for the conventional cubic NES with $\gamma = 0.3$ and $G(b) = \frac{3b^2}{4}$ (see (B.1)) and finally the red curves refer to the SIM for the novel NESs of different values

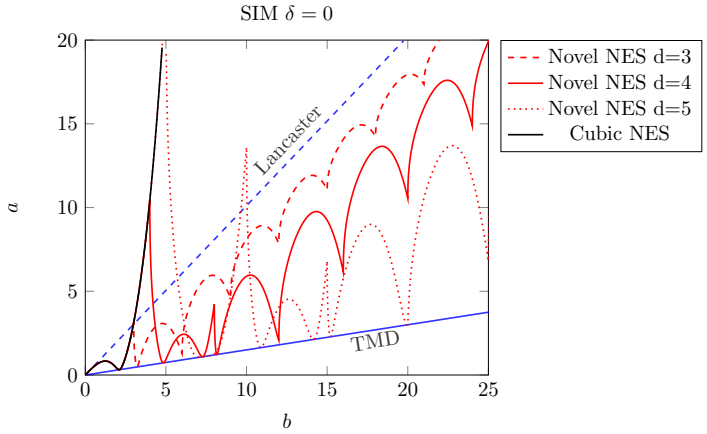

Figure 2: The slow invariant manifold for TMD, Lancaster damper, cubic NES and the novel NES for $\xi_{\text{na}} = 0.15$, $\delta = 0$ and $\gamma = 0.3$.

d. It is observed that:

- The TMD and Lancaster damper SIMs are straight lines and form a funnel.
- The NESs' SIMs for $a \to 0$ are close to the Lancaster line, and have a local minimum that touches the TMD line.
- The novel periodically extended NES's SIM is equal to the cubic NES's SIM until d, where it branches down, touching the TMD line, and staying for the most part within the funnel constructed by Lancaster and TMD lines. The periodically softening and hardening of the stiffness thus moves the SIM more to the right.
- The novel NES' SIM moves to the right for increasing d.

3.4. SIM dynamics and stability

The SIM in (14) was found with relatively few calculations. However, it does not convey the dynamics along the SIM or the stability of the solutions plot in Figure 2. A procedure to obtain this for other type of NES configurations and stiffness characteristics is found in [13, 35, 34]. First, the compound system's dynamics are analyzed on two time scales, where the fast time the stability of the SIM branches. and the slow time will yield the same expression as (14) and dynamics on the SIM. The following is applied to the primary system dynamics (5) after change of coordinates (6) and (7) and is applied to the absorber equation (8) (with $\kappa = 0$) :

$$\begin{aligned} A(\tau) &= A(\tau_1, \tau_2) \quad \tau_0 = \tau,\ \tau_1 = \epsilon\tau \\ \frac{d}{dt} &= \frac{\partial}{\partial \tau_0} + \epsilon \frac{\partial}{\partial \tau_1} \end{aligned} \tag{17}$$

Subsequently harmonic balancing and then collecting in terms of order ϵ^0 yields:

$$\begin{aligned}
&\frac{\partial A}{\partial \tau_0} = 0 \\
&\frac{\partial B}{\partial \tau_0} + \cancel{\frac{\partial A}{\partial \tau_0}} + \frac{\xi_{\text{na}}}{\sqrt{1+\delta}}\frac{B}{2} + \frac{\gamma}{1+\delta}\frac{B \cdot G(B,\bar{B})}{2j} - \frac{B}{2j} - \frac{A}{2j} = 0
\end{aligned} \tag{18}$$

which express the 'fast' dynamics. Linearizing (18) around equilibrium $B = B^* + \Delta_B$ eventually results in the following system of linear equations in Δ_B and $\bar{\Delta}_B$:

$$\begin{bmatrix} \dot{\Delta}_B \\ \dot{\bar{\Delta}}_B \end{bmatrix} = \underbrace{\begin{bmatrix} a_{11} & a_{12} \\ a_{21} & a_{22} \end{bmatrix}}_{\mathbf{\Sigma}} \begin{bmatrix} \Delta_B \\ \bar{\Delta}_B \end{bmatrix} \tag{19}$$

where

$$\begin{aligned}
a_{11} &= \bar{a}_{22} - \frac{j}{2} - \frac{\xi_{na}}{2} + \frac{j}{2}\left.\frac{\partial(B \cdot G(B,\bar{B}))}{\partial B}\right|_{B=B^*} \\
a_{12} &= \bar{a}_{21} = \frac{j}{2}\left.\frac{\partial(B \cdot G(B,\bar{B}))}{\partial \bar{B}}\right|_{B=B^*}
\end{aligned} \tag{20}$$

The expressions for $\frac{\partial(B \cdot G(B,\bar{B}))}{\partial B}$ and $\frac{\partial(B \cdot G(B,\bar{B}))}{\partial \bar{B}}$ are found in Appendix C. If any eigenvalue of $\mathbf{\Sigma}$ has a positive real part, then the fixed point $B = B^*$ is unstable. The fixed point B^* lay on the SIM of (14) with the phase determined from (12). Figure 3 illustrates the stability of the SIM for the novel NES, for various values of d. It can be noticed that unstable and stable branches are separated by folds, as expected from obvious topological considerations. This analysis identified no other source of instability. The dynamics along the SIM are obtained by collecting the primary system equation for order ϵ^1 after applying (17) and harmonic balancing:

$$\frac{\partial A}{\partial \tau_1} + \frac{\xi}{\sqrt{1+\delta}}\frac{A}{2} + \frac{\partial B}{\partial \tau_0} - \frac{B}{2j} - \frac{A}{2j} = 0 \tag{21}$$

Then, assuming the dynamics only on a slow time scale (s.t. $\frac{\partial B}{\partial \tau_0}$) and plugging in the second equation of (18):

$$\frac{\partial A}{\partial \tau_1} + \frac{\xi}{\sqrt{1+\delta}}\frac{A}{2} - \frac{\xi_{\text{na}}}{\sqrt{1+\delta}}\frac{B}{2} - \frac{\gamma}{1+\delta}\frac{B \cdot G(B,\bar{B})}{2j} = 0 \tag{22}$$

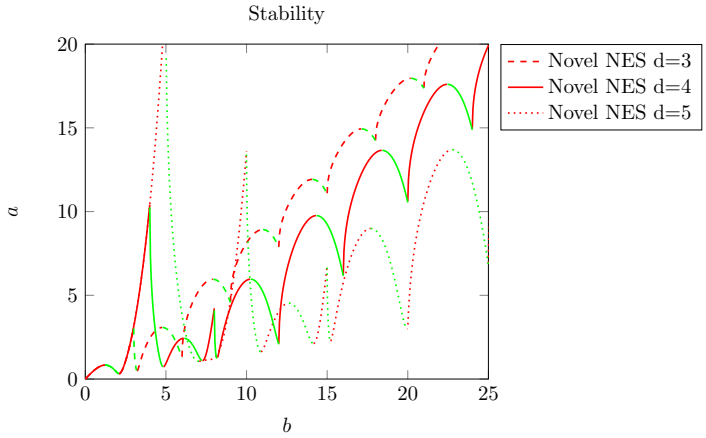

Figure 3: Stability of the SIM for d=3, d=4 and 5 where red are stable branches and green are unstable branches, for $\xi_{\text{na}} = 0.15$, $\delta = 0$ and $\gamma = 0.3$.

After that, substituting $A = ae^{j\alpha}$ and $B = be^{j\beta}$, the real part of (22) and the real and imaginary part the second equation of (18) on a slow time scale becomes:

$$\begin{aligned} &\frac{\partial a}{\partial \tau_1} + \frac{\xi}{\sqrt{1+\delta}}\frac{a}{2} - \frac{\xi_{\text{na}}}{\sqrt{1+\delta}}\frac{b}{2}\sin(\beta-\alpha) = 0 \\ &-\frac{a}{2}\sin(\alpha-\beta) + \frac{\xi_{\text{na}}}{\sqrt{1+\delta}}\frac{b}{2} = 0 \\ &\frac{a}{2}\cos(\alpha-\beta) + \frac{\gamma}{1+\delta}\frac{b\cdot G(b)}{2} - \frac{b}{2} = 0 \end{aligned} \tag{23}$$

Then inserting the second equation in the first, and adding the square of the second and third equation of (23) leads to:

$$\begin{aligned} \frac{\partial a^2}{\partial \tau_1} &= -\frac{\xi}{\sqrt{1+\delta}}a^2 - \frac{\xi_{\text{na}}}{\sqrt{1+\delta}}b^2 \\ a^2 &= \left(\frac{\xi_{\text{na}}^2}{1+\delta} + \left(1 - \frac{\kappa}{1+\delta} - \frac{\gamma}{1+\delta}G(b)\right)^2\right)b^2 \end{aligned} \tag{24}$$

The first equation in (24) states that the primary system vibration amplitude squared, will decrease if there is damping. The second is the SIM derived previously in (14).

3.5. Dissipation power

To quantify the performance of the NES, the dissipation power is now considered. This quantity is the power of dissipation by the viscous damper of the

absorber. In (5), the damping coefficient is $\frac{\epsilon\xi_{\mathrm{na}}}{\sqrt{1+\delta}}$, which has an averaged per period dissipation power of $P_{\mathrm{diss}}(\tau) = \frac{\epsilon\xi_{\mathrm{na}}}{\sqrt{1+\delta}}b^2$ [16, 36]. As the dissipation power is proportional to the square of the relative NES amplitude of vibration, the SIM also expresses the performance of an NES. This means that the higher the NES amplitude b for a given primary system vibration a, the higher the dissipation power is. Referring to the SIMs in Figure 2, the more to the right a SIM is for a certain a, the higher its dissipation power is and the faster the associated vibration absorber will dissipate vibrations. For a certain absorber damping ξ_{na}, a given vibration amplitude a and a fully known primary system $\delta = 0$, the SIMS (15) and (14) give the absorber vibration amplitudes. It is now shown that the TMD will always have a higher amplitude b as:

$$\begin{aligned} a^2 =& \xi_{\mathrm{na}}^2 b_{\mathrm{TMD}}^2 = \left(\xi_{\mathrm{na}}^2 + (1-\gamma G(b_{\mathrm{NES}}))^2\right) b_{\mathrm{NES}}^2 \\ \Rightarrow =& \frac{b_{\mathrm{NES}}^2}{b_{\mathrm{TMD}}^2} = \frac{\xi_{\mathrm{na}}^2}{\xi_{\mathrm{na}}^2 + (1-\gamma G(b_{\mathrm{NES}})^2} \leq 1 \end{aligned} \tag{25}$$

Thus, under the assumption of 1:1 resonance and a certain primary system ($\delta = 0$), any NES will dissipate energy slower than the TMD provided they have the same ξ_{na}. Considering that the NES is generally more complex to realize and to analyze than a linear absorber, if the SIM of an NES lies above the funnel between the SIMs of the TMD and of the Lancaster absorber, it should be considered unacceptable, as then a more simpler device (mass and viscous damper) is better than the NES. In the next section, it is investigated under what conditions an NES can be better for an uncertain primary system where $\delta \neq 0$, but first it is investigated if the SIM for the novel NES is representative for the actual vibrations by comparison with numerical simulations.

3.6. Simulations

An undamped primary system having mass $m = 1$ kg and assumed stiffness $k_{\mathrm{a}} = 1$ N/m, without uncertainty ($\delta = 0$) is fitted with a vibration absorber with mass ratio $\epsilon = 0.02$ and damping $\xi_{\mathrm{na}} = 0.15$. The absorbers compared here are a TMD, a cubic NES with $\gamma = 0.3$ and the novel periodically extended NES with $\gamma = 0.3$ and $d = 4$. Different transient conditions are now investigated.

3.6.1. $\dot{x}(0) = 1$ m/s

In a first simulation presented in Figure 4, the primary system is impulsively excited with $\dot{x}(0) = 1$ m/s. The primary system's and absorber's vibrations are shown in Figure 4a and 4b, respectively. The TMD produces the fastest vibration decay. For the NESs, the vibration decays significantly but an amount of residual energy remains. The vibrations of the novel and cubic NES overlaps because the NES' vibration amplitude stays below $d = 4$, thus the periodical

extensions of the novel NES are not activated. The vibration envelopes of the simulations are given in Figures 4c and 4d, where $a(t) = \sqrt{\omega_1^2 x^2(t) + \dot{x}^2(t)}$ and $b(t) = \sqrt{\omega_1^2 z^2(t) + \dot{z}^2(t)}$. These contain the same information as the vibrations itself. Finally, the envelopes of the simulations are compared to the SIMs in Figure 4e. Apart from the initial part of the simulation, where transient dynamical phenomena take place, all the envelopes follow quite accurately the SIM derived analytically. The small increase in the vibration amplitude of the primary system after the initial rapid decrement (at $t = 40$ s in Figure 4c and at $t = 50$ s in Figure 4d) is related to a linear beating phenomenon.

3.6.2. $\dot{x}(0) = 3$ m/s

The results of the simulations related to the initial condition $\dot{x}(0) = 3$ m/s are shown in Figure 5. The vibrations are depicted in Figures 5a and 5b. The envelopes of the primary system shown in Figure 5c prove that also for this larger initial velocity, the TMD is the best absorber. As the primary system and the TMD are linear, their response are just a scaled version of the previous simulation. However, now the performance of the cubic NES is much worse than the novel periodically extended NES. The reason for this is because the novel NES' amplitude is higher than the cubic NES, as seen in the envelope of the NES, Figure 5d. By comparing the SIMs with the envelopes in Figure 5e, it is seen that the novel NES's envelope is attracted by those branches of the SIM having a higher dissipation power. The conventional cubic NES stays on its SIM which generates a much slower dissipation, having lower b values. Also, it can be seen that for $a \approx 1.1$, the novel NES's vibration envelope jumps back to the SIM of the cubic NES. This is visible in the envelopes as the decay slows down starting from 70s in Figure 5c and the absorber's vibration amplitude suddenly decreases in Figure 5d.

3.6.3. $\dot{x}(0) = [5, 7, 10]$ m/s

For the next three simulations, only the primary system's envelope and the comparison of the SIM and the envelopes are illustrated. The time evolution of the envelopes in Figures 6a to 6c show that while the decay with TMD just scales in amplitude, the decay with cubic NES becomes slower with increasing excitation and that the novel NES, although worse than the TMD, significantly outperform the conventional NES. The envelopes follow the SIMs quite well, as illustrated in Figures 6d to 6f, which confirms the predictive character of the SIM. The novel NES jumps from branch to branch as it descends the SIM. The better performance of the novel NES compared to the conventional NES is clearly related to the position of the corresponding SIM further to the right. The simulations performed so far clearly illustrate that the conventional NES has a limited energy bandwidth, which the novel NES extends significantly.

3.6.4. SIM and filtered response $\dot{x}(0) = [10, 20]$ m/s

In the comparison of the SIM (red) and fast dynamics (red-dotted) for the novel NES in Figures 4e, 5e and 6d-6f, it is hard to see jumps from branch to branches. This is because while the SIM assumes an 1:1 resonance, the vibrations of the NES may contain other sub- or superharmonics. Therefore, Figure 7 has band-pass filtered versions of the NES vibrations in green to investigate the 1:1 part of the response. The filter only keeps frequencies between $0.8\omega_0$ and $0.2\omega_0$. The resemblance of the SIM and simulation is more clear, where the vibrations on average follow the SIM. Furthermore, the jumps of the vibrations go from stable to stable branch, avoiding the unstable branches. This is as predicted from the stability analysis in Figure 3.

3.6.5. Dissipation time

The performance in the simulations above was only qualitatively assessed. To quantify the performance, the dissipation time under different loading is now computed. The 70% dissipation time is defined as the time required for dissipating 70% of the initial total energy $E_{tot}(t)$:

$$T_{\text{diss},70\%} = \{t \in \mathbb{R}_+ : E_{\text{tot}}(t) = 0.3 \cdot E_{\text{tot}}(0)\} \tag{26}$$

where the total energy is the sum of the kinetic and potential energy in the system:

$$E_{\text{tot}}(t) = \frac{m\dot{x}(t)^2}{2} + \frac{m_{\text{na}}\dot{x}_{\text{na}}(t)^2}{2} + \frac{k(1+\delta)x(t)^2}{2} + k_{\text{na}} \int_0^{|x-x_{\text{na}}|} F(z)dz \tag{27}$$

This $T_{\text{diss},70\%}$ is now computed for the primary system with attached either the TMD, NESs considered previously and also the Lancaster damper; furthermore, various values of d (namely d=3, 4 or 5) are considered for the novel NES. The results are shown in Figure 8. The TMD's dissipation time is 24.8 s and does not alter under increased excitation. The conventional cubic NES's dissipation time increases from about 58 s for $\dot{x}(0) = 1$ m/s to over 3000 s for $\dot{x}(0) = 20$ m/s. The performance of novel NESs at first follows the curve of the cubic NES, however, increasing the initial energy, it significantly differs from it. The novel NES with $d = 3$ is the first one to jump down from the cubic NES's performance line, followed by the novel NES with $d = 4$ and finally by the novel NES with $d = 5$. However, once the novel NESs dissipation time jumps down from cubic NES, the novel NES with larger d performs better than the novel NES with smaller d values, i.e. $d = 3$ performs worst and $d = 5$ best. This was already predicted by the SIMs on Figure 2, where SIMs of the novel NESs with a higher d are more to the right and thus will have a better dissipation time.

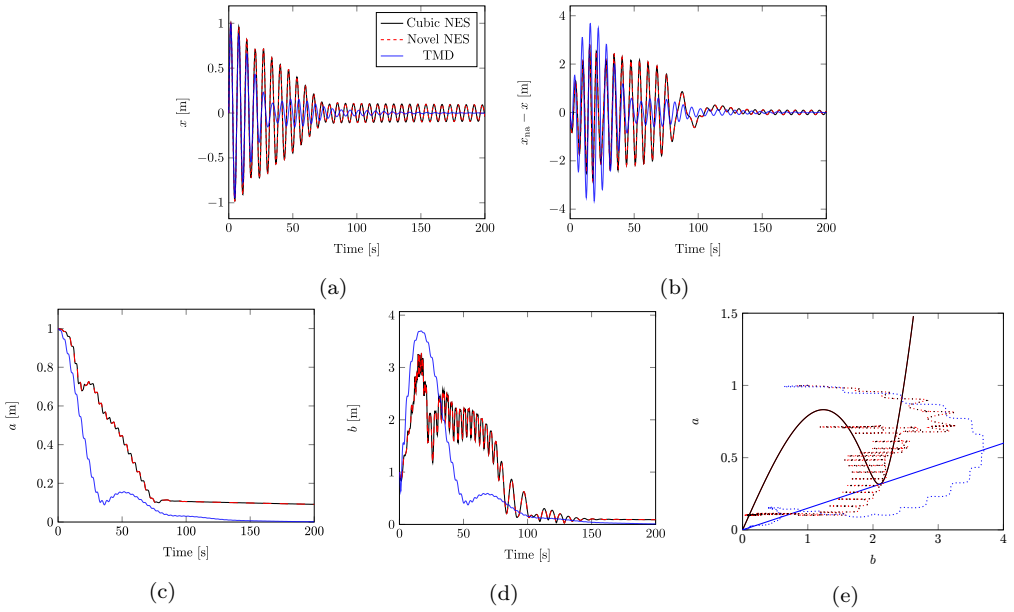

Figure 4: Simulation results for $\dot{x}(0) = 1$ m/s, with (a) the primary system's vibration, (b) the absorber's vibration, (c) the vibration envelopes of (a), (d) the vibration envelopes of (b) and (e) a comparison of SIMs and the envelope of vibrations (c) and (d) where the solid line are the SIMs and the dashed the simulations. For these simulation, $\omega_0 = 1$ rad/s , $\delta = 0$, $\epsilon = 0.02$, $\xi_{\mathrm{na}} = 0.15$, $\gamma = 0.3$ for the two NESs and $d = 4$ for the novel NES.

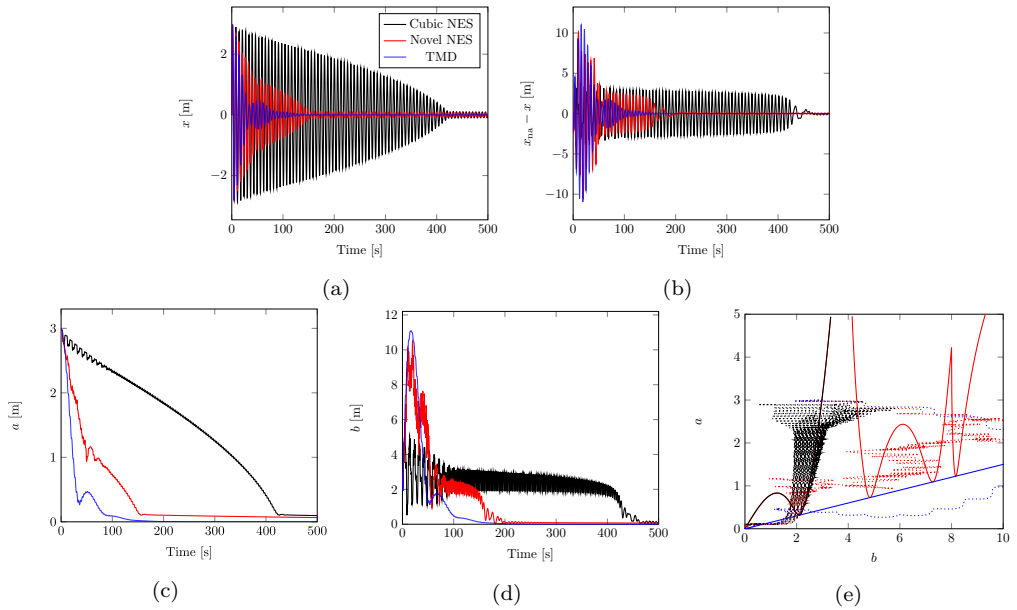

Figure 5: Simulation results for $\dot{x}(0) = 3$ m/s, with (a) the primary system's vibration, (b) the absorber's vibration, (c) the vibration envelopes of (a), (d) the vibration envelopes of (b) and (e) a comparison of SIMs and the envelope of vibrations (c) and (d) where the solid line are the SIMs and the dashed the simulations. The same primary system and NES parameters as for Figure 4 are used.

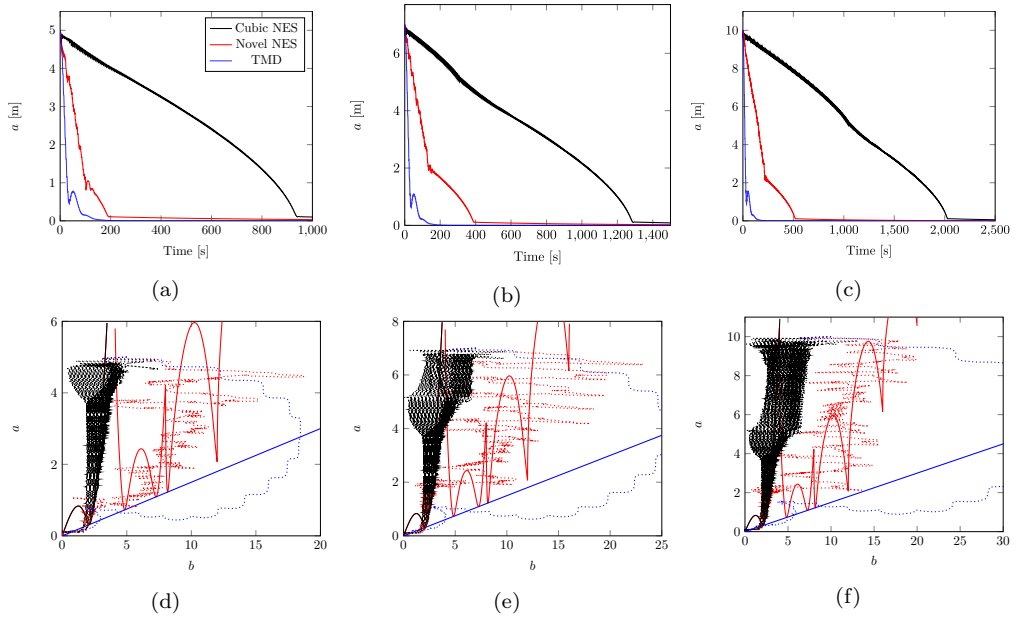

Figure 6: Primary system's envelope for $\dot{x}(0) = [5, 7, 10]$ m/s (a),(b),(c) and compared to SIM (d)(e)(f). The same primary system and NES parameters as for Figure 4 are used.

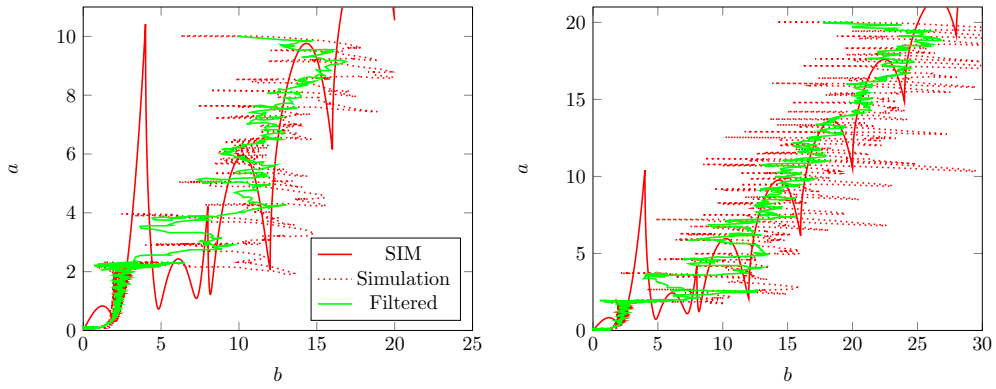

Figure 7: Comparing filtered simulations to the SIM, for $\dot{x}(0) = 10$ m/s (a) and $\dot{x}(0) = 20$ m/s, for a 1:1 comparison.

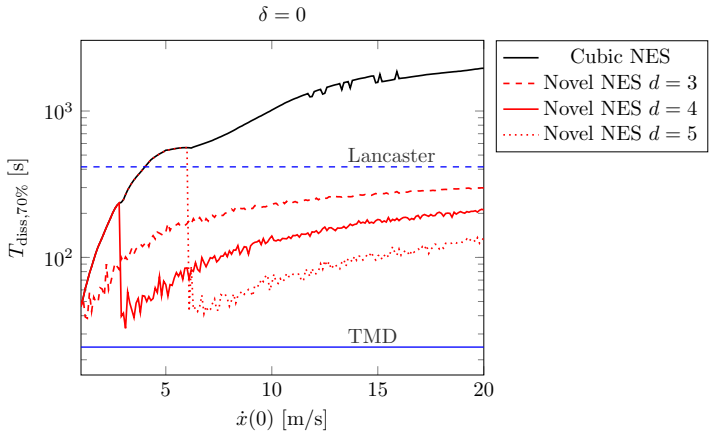

Figure 8: The 70 % dissipation time of the cubic NES, the novel NES and TMD for $\delta = 0$. To calculate this, $\omega_0 = 1$ rad/s , $\delta = 0$, $\epsilon = 0.02$, $\xi_{\text{na}} = 0.15$, $\gamma = 0.3$ for the two NESs.

4. Uncertain primary system

The dynamical system in (3) has an uncertainty on the primary stiffness, expressed in δ. This δ is now varied from -0.4 to 0.4. The SIMs will be analyzed to predict performance, and then the 70% dissipation time will be computed to verify this prediction.

4.1. SIMs

The SIMs for an uncertainty of $\delta = -0.2$ are plotted in Figure 9a. The SIM for the cubic NES and all of the SIMs for the novel NES dip below the line of the TMD. This means, that for certain intervals of a, the TMD is not the best DVA to dissipate the vibrations. As was seen before, periodically extended NESs with larger d, perform better. By decreasing δ to -0.4, the SIMs in Figure 9b show that the TMD's performance deteriorates even more. The periodically extended NES with $d = 4$ and $d = 5$ stay below the TMD line for a large range of the plotted interval.

The effect of a positive uncertainty $\delta = 0.2$ on the SIMs is plotted in Figure 9c. The NESs also dip below the TMD line, but only for short intervals. Increasing the uncertainty δ to 0.4, Figure 9d, increases these intervals, but the TMD still seems to be a better DVA for the most part. To support the predictions made by the SIMs, the 70% dissipation time is now computed from simulations.

4.2. Dissipation time

To verify the performance, the 70% dissipation time is determined and depicted in Figure 10. For $\delta = -0.2$ (Figure 10a) the dissipation time for the NES shift closer to the TMD line compared to $\delta = 0$ (Figure 8). The cubic NES's performance quickly deteriorates, however the periodically extended NESs outperform the TMD for a certain energy bandwidth. For $\delta = -0.4$, see Figure 10b, the TMD's performance is subpar compared to the NESs. This was predicted by the SIMs in Figure 9b. The periodically extended NES performs better when d increases. However, the dissipation time for the periodically extended NESs follows the curve of the cubic NESs for a wider range than for $\delta = -0.2$, before then jumping below the TMD line.

Finally, for positive δ, Figures 10c for $\delta = 0.2$ and 10d for $\delta = 0.4$ reveal that for the majority of the energy bandwidth considered the TMD still outperforms all the NES considered.

These results illustrate how the performance of the TMD rapidly decreases if its natural frequency is larger than the natural frequency of the primary system ($\delta = -0.2$ and -0.4). Conversely, the TMD is still relatively efficient if its natural frequency is smaller than the natural frequency of the primary system ($\delta = 0.2$ and 0.4). These conclusions suggest that, in order to remain efficient under

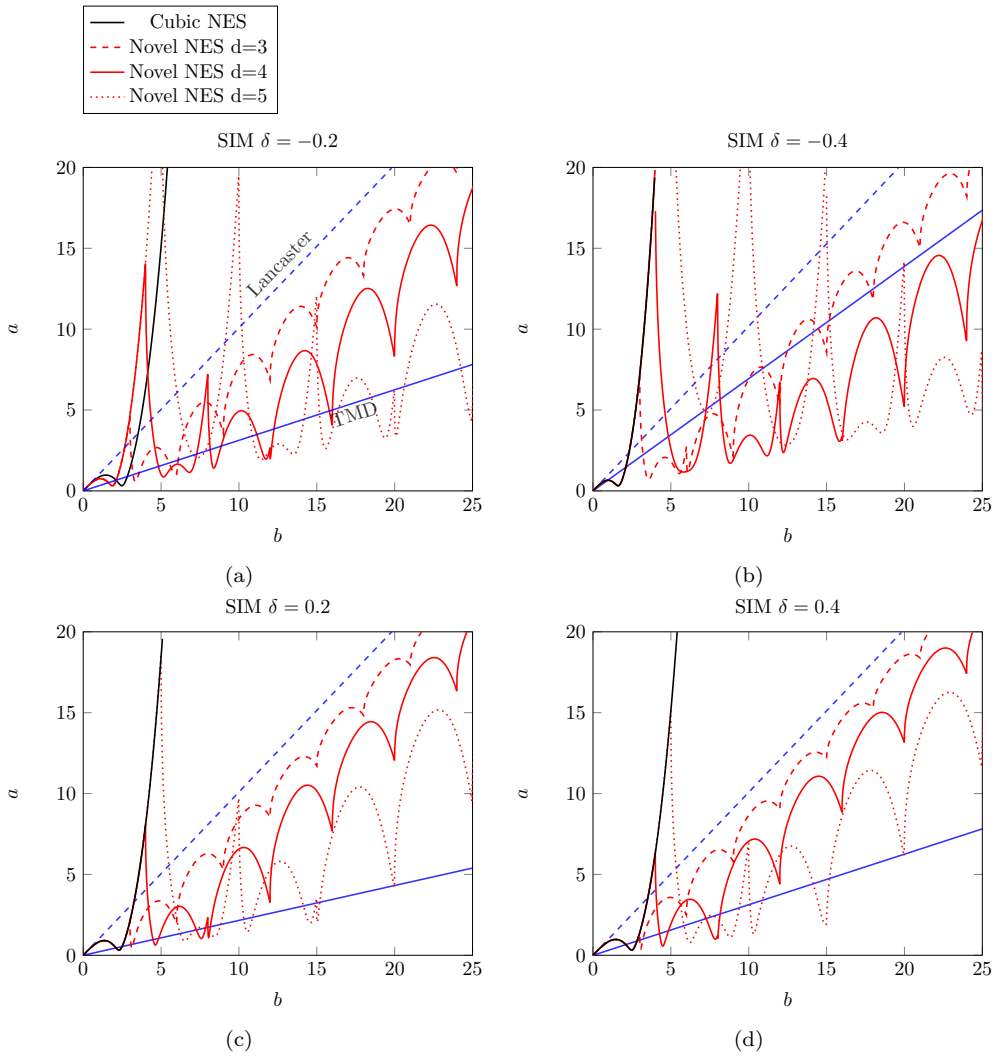

Figure 9: SIMS for the TMD, Lancaster damper, cubic NES and the novel periodically extended NES for uncertain primary system where $\delta = -0.2$ (a), $\delta = -0.4$ (b), $\delta = -0.2$ (c) and $\delta = -0.4$ (d). Other parameters are $\xi_n a = 0.15$ and $\gamma = 0.3$.

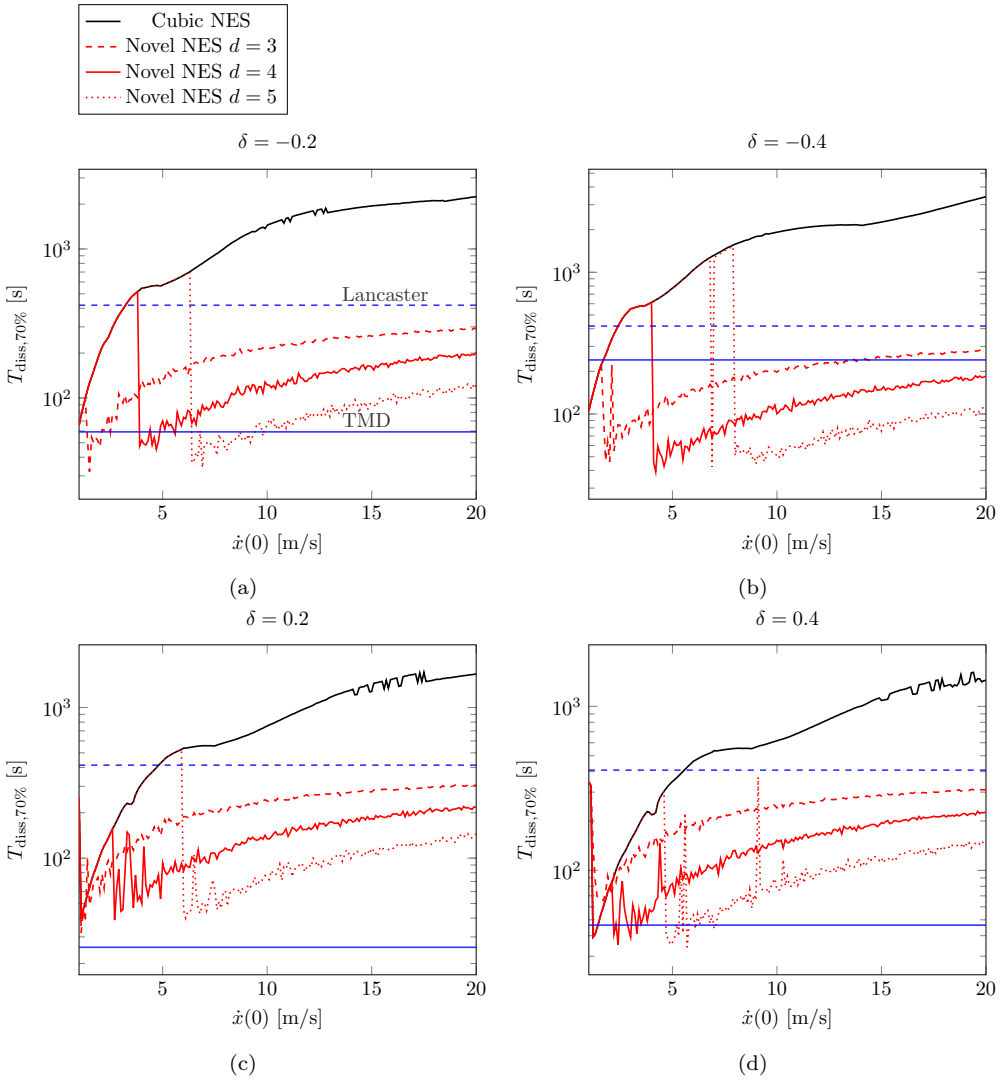

Figure 10: Dissipation time for the TMD, cubic NES and the novel periodically extended NES for uncertain primary system where $\delta = -0.2$ (a), $\delta = -0.4$ (b), $\delta = 0.2$ (c) and $\delta = 0.4$ (d). Additionally, $\omega_0 = 1$ rad/s , $\delta = 0$, $\epsilon = 0.02$, $\xi_{\text{na}} = 0.15$, $\gamma = 0.3$ for the two NESs.

variations of the natural frequency of the primary system, the natural frequency of the TMD should be decreased. The analysis performed does not disclose if, in that case, the cubic or the novel NES are more efficient than the TMD.

In order to provide a fair comparison between the three absorbers, in the next section, the parameter values of the absorbers are optimized for specific ranges of energetic levels and uncertainty, then their dissipation times are compared.

4.3. Optimized absorbers for an uncertain primary system

In this section, we perform an optimization of the absorbers' parameters for the TMD, the cubic NES and the novel NES considering that $\delta \in (-0.4, 0.4)$ and that $\dot{x}(0) \in (5, 10)$ m/s. The optimization is performed adopting the worst-case-scenario approach, meaning that, for each configuration of the absorber (each set of ξ_{na}, κ, γ and d values), the largest dissipation time $T_{\text{diss},70\%}$ over the full range of parameters δ and $\dot{x}(0)$ is considered. This analysis will enable us to compare the three absorbers when they are explicitly designed to stand positive and negative uncertainties of the primary system and a specific range of initial energy level.

In the case of the TMD and of the cubic NES, only the damping coefficient ξ_{na} and the absorber's stiffness coefficients – κ or γ, respectively – must be optimized (the mass ratio is assumed fixed at 0.05). Therefore, the optimization is performed by calculating the dissipation time, through direct numerical simulations, over a grid of values in the κ, ξ_{na} and γ, ξ_{na} spaces, respectively. 20 equally spaced intervals of $\dot{x}(0)$ ranging from 5 to 10 m/s, while only the cases of $\delta = -0.4$ and $\delta = 0.4$ were considered, in order to reduce computational time. Intermediate values of δ were investigated only for validating the optimal configurations obtained. Although the choice of the initial energy values might seem arbitrary, the TMD is amplitude-invariant because of its linearity, while for the NES, variations of the vibration amplitude scale with the nonlinear stiffness (see [11]). Therefore, any energy level is equivalent, as far as the stiffness is tuned accordingly. On the contrary, the ranges of variation of the initial energy and δ are indeed arbitrary. The results of the computation are illustrated in Figure 11.

From the figure, the better performance of the TMD over the NES is clearly visible. The worst dissipation time obtained with the optimally tuned TMD is 25.3 s, while the NES is unable to provide a worst-case dissipation time lower than 43.65 s, which is almost double. Looking at the parameter values required for minimizing the dissipation time (marked by red dots in Figure 11), we notice that the TMD can enlarge the frequency range of effectiveness by reducing its natural frequency ($\kappa = 0.668$) and adopting relatively large damping ($\xi_{\text{na}} = 0.394$). The optimal NES has an even higher damping $\xi_{\text{na}} = 0.667$, while its dimensionless cubic stiffness coefficient γ is very small ($\gamma = 0.014$). This result shows that a properly tuned TMD is indeed able to operate on a relatively large frequency

band. Similar conclusions were drawn for a TMD mitigating forced vibrations of a primary system with uncertainties [37].

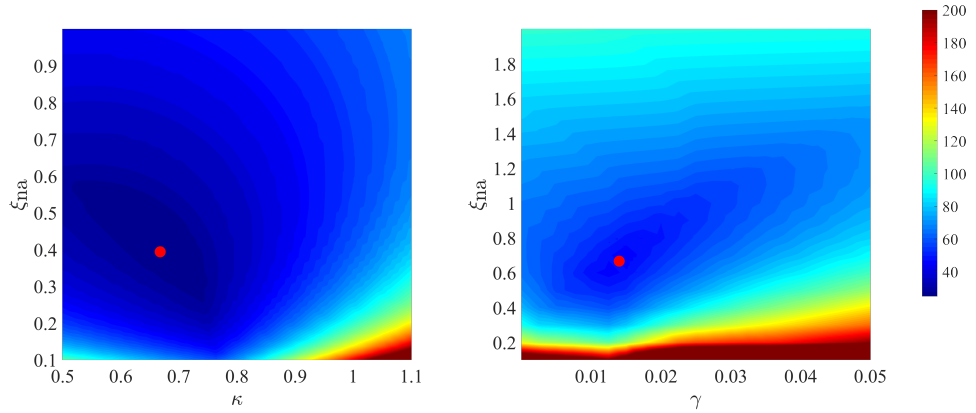

Figure 11: Dissipation time for the TMD (a) and for the cubic NES (b) for $\epsilon = 0.05$. The colors indicate the largest dissipation time for the initial conditions $\dot{x}(0) \in (5,\ 10)$ m/s and $\delta = \pm 0.4$. The slowest dissipation times are marked by the red dots. Simulations where limited to 200 s.

The optimization of the novel NES is more complicated. In fact, there are three parameters to be optimized (ξ_{na}, γ and d) and analyzing the dissipation times on a dense enough 3-dimensional grid for the three parameters is computationally too demanding for the available resources. An initial attempt to find the optimal parameters through the simplex search method [38] revealed itself to be strongly dependent on the initial guess; therefore, this procedure was discarded, and a genetic algorithm was applied instead. Considering the d value ranging between 1 and 8 and repeating the computation several times, two significantly different local optima were obtained, having the values indicated in the first two columns of Table 1.

Optimum 1		Optimum 2	
ξ_{na}	0.44	ξ_{na}	0.422
γ	2.033	γ	0.216
d	1.88	d	4.091
$T_{\text{diss},70\%}$	31.26	$T_{\text{diss},70\%}$	31.39

Table 1: Sets of optimal parameter values for the novel NES.

The parameter values of the two optima are very scattered, apart from the damping ξ_{na}, which is similar to the optimal value obtained for the TMD (≈ 0.4), but significantly smaller than the damping required for the optimal cubic NES ($\approx$

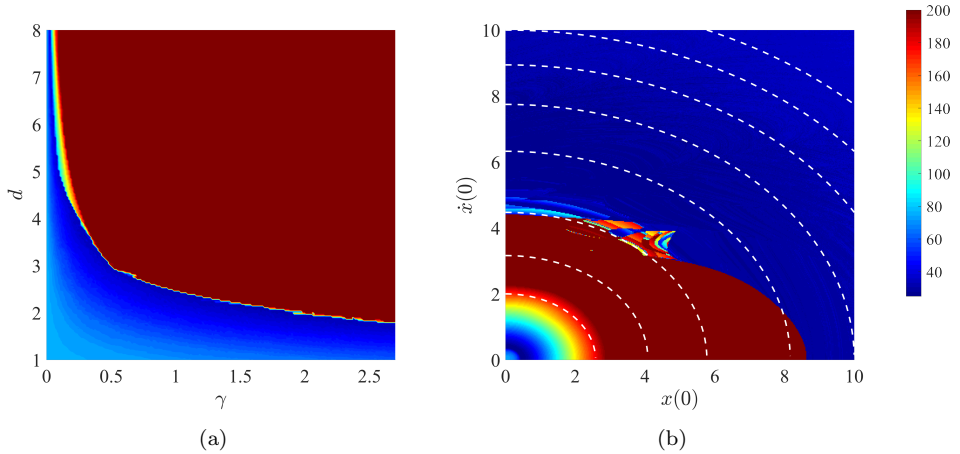

Figure 12: (a) Dissipation time for the periodic NES for $\xi_{\mathrm{na}} = 0.44$ (worst-case-scenario approach). (b) Dissipation time, for various initial conditions, for the periodic NES with parameter values as in Table 1 (Optimum 1) and $\delta = -0.4$; white dashed lines mark curves with equal initial energy. Simulations where limited to 200 s.

0.7). Dissipation time is around 31 s, which is much smaller than the dissipation time of the cubic NES (43.65 s). However, according to this analysis, the TMD outperforms both the NESs considered for the given range of uncertainty and initial conditions.

In order to better understand the effect of the parameter values on the performance of the novel NES for an uncertain primary system, we compute the dissipation time on a section of the three-dimensional parameter space ξ_{na}, γ, d, for $\xi = 0.44$. This corresponds to the first optimum in Table 1. The resulting diagram is illustrated in Figure 12a. Also this computation considers the worst-case scenario for the same variations of $\dot{x}(0)$ and δ.

The figure depicts a quite peculiar structure. The points providing the lowest dissipation times are organized along a curve that resembles a hyperbola. On this curve, the dissipation time is relatively homogeneous and varies approximately between 30 and 35 s. A technical consequence of this observation is that the optimal design of this NES leaves some freedom, exploitable to overcome practical constraints over the values of γ and d. However, we also notice that this curve marks a sort of boundary of a parameter space region with very large dissipation time and poor performance, existing for γ values above this curve.

This sharp variation is clearly related to a significant difference in the dynamics of the two cases (slow and fast dissipation), which is most probably related to the multiple coexisting SIM stable branches. If more than one stable branch of the SIM exists for a given value of the primary system oscillation amplitude a, the slow dynamics of the system may converge to any of the branches, depending

on the initial conditions of the system. Branches on the left provide slower energy dissipation than branches on the right.

In order to verify this hypothesis, we computed the dissipation time for a fixed configuration of the novel NES – corresponding to the first optimum – utilizing a grid of initial conditions of the primary system, involving not only initial velocity but also initial displacements. For the computation, δ was fixed at -0.4. The result is depicted in Figure 12b. The color map in the figure indicates the dissipation time, while dashed white lines mark curves with constant initial energy. The figure illustrates that dissipation time can abruptly change for precisely the same absorber tuning and initial energetic level. This is a clear sign that different distributions of the energy on the primary system can lead the system to different coexisting branches of the SIM, with very different dissipation properties. This behavior is hardly predictable since variations in the initial conditions can always occur unexpectedly. Nevertheless, the variation of dissipation time, even if sudden and sharp, approximately follows the isoenergetic curves. This means that, although uncertainties exist, it is still possible to tune the novel NES for a target energy range quite safely.

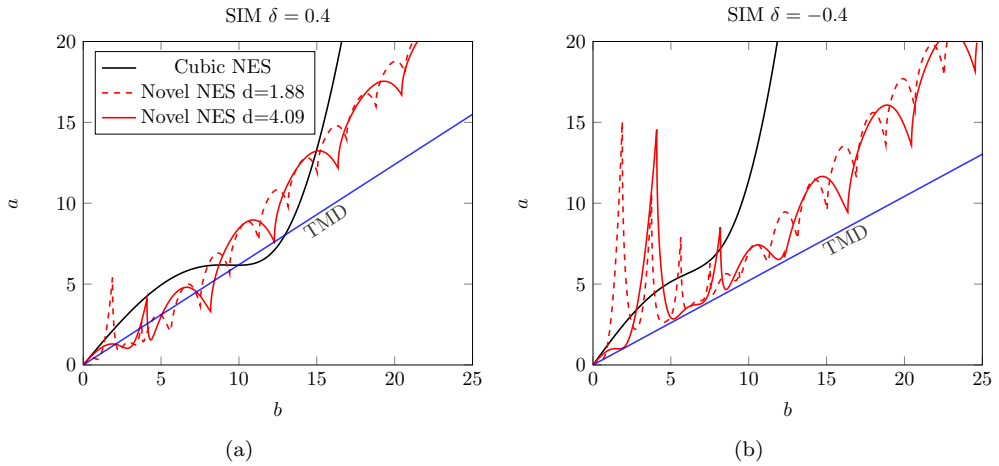

Figure 13: SIMs of the optimal TMD ($\xi_{\text{na}} = 0.394$, $\kappa = 0.668$), optimal conventional NES ($\xi_{\text{na}} = 0.667$, $\gamma = 0.0.014$) and the first two novel NESs from Table 1. The SIMs in (a) have $\delta = 0.4$ and in (b) $\delta = -0.4$.

The SIMs of the optimized TMD, conventional NES and novel NESs are presented in Figure 13 for $\delta = 0.4$ and $\delta = -0.4$. For $\delta = 0.4$, the SIMs for the conventional and novel NESs dip below the TMD line. However, for $\delta = -0.4$, this is not the case. This confirms that for the range of $\delta \in [-0.4, 0.4]$, the optimal TMD is more robust than the others for worst-case scenario optimization.

5. Conclusion

This paper explored a nonlinear energy sink (NES) with a novel stiffness characteristic, the periodically extended cubic stiffness. Its performance in mitigating transient vibrations of an uncertain single-degree-of-freedom primary system was investigated by deriving a slow invariant manifold (SIM), by assuming a 1:1 resonance between the primary system and the NES. The SIM is a static expression, that relates the vibration amplitude of the primary system to that of the NES, and can predict the power dissipation of the NES, while also being computationally efficient, as no numerical integration is needed. The SIMs of the novel NES were compared to the SIMs of the conventional cubic NES, of the tuned-mass-damper and of the Lancaster damper. The SIMs showed that for primary systems that do not have any uncertainty, the TMD has the largest dissipation power in 1:1 resonance, when compared to an NES, regardless of its stiffness characteristic. The SIM also revealed that the conventional NES have a very small energy bandwidth where it performs well; on the contrary, the novel periodically extended NES significantly increases this energy bandwidth. Furthermore, the SIMs clearly illustrated that the SIMs of the Lancaster damper and of the TMD form a funnel. The SIM of the NES is, for low amplitude, tangent to the SIM of the Lancaster damper, while for a certain energy level it is tangent to the SIM of the TMD. For higher energy levels, the SIM of the cubic NES lies outside this funnel, above the Lancaster damper line, making the NES inefficient for that energy level; while the newly proposed NES possesses a SIM which lies below the Lancaster line for almost any energy level.

For primary systems with an uncertainty on the stiffness, the SIMs revealed that performance of a regular TMD deteriorates, while the periodically extended NES's performance is more robust and, in some cases, even better than that of the TMD. By increasing the period of the periodic extension, the performance increased even further. To confirm the predictive properties of the SIM, numerical simulations were performed comparing the cubic NES, the periodically extended NES and the TMD. On thereof obtained time evolutions, the 70% dissipation time was computed. The simulations showed that the SIM is a good representation of the vibration amplitude and is a good predictor of the actual performance of the investigated vibration absorber, therefore they confirmed the results analytically predicted. By performing an optimization of the TMD, the cubic NES and the periodically extended NES explicitly designed for mitigating vibrations of primary systems encompassing large uncertainty range, it was shown that the TMD, if properly tuned, can dissipate vibrations over a relatively large frequency range, significantly outperforming the cubic NES. In the future, the performance of the novel NES for multi degrees-of-freedom primary systems and for other types of excitations, such as harmonic or random, should be investigated.

This research, focused on a specific shape of the restoring force of the absorber,

showed that the energy bandwidth of an NES can be significantly increased. Indeed, the objective of the research was to illustrate that NESs encompassing unconventional restoring forces can have enhanced performance. Nevertheless, the chosen periodically extended restoring force is certainly not the optimal one and infinitely many others can be proposed. In this context, we believe that future researches in the topic should not consider a specific uncommon restoring force, but should rather aim at identifying the optimal possible restoring force shape, by exploiting analytical tools such as the SIM and numerical optimization.

Acknowledgements

Giuseppe Habib acknowledges the financial support of the Hungarian National Science Foundation under grant number OTKA 134496 and of the NRDI Fund (TKP2020 NC, Grant No. BME-NC) based on the charter of bolster issued by the NRDI Office under the auspices of the Ministry for Innovation and Technology.

References

[1] H. Frahm, Device for damping vibrations of bodies (U.S. Patent 9 899 58A, 10/1909).
[2] J. Den Hartog, J. Ormondroyd, Theory of the dynamic vibration absorber, ASME J. Appl. Mech 50 (7) (1928) 11–22.
[3] O. Gendelman, L. Manevitch, A. F. Vakakis, R. Mcloskey, Energy pumping in nonlinear mechanical oscillators: Part i dynamics of the underlying hamiltonian systems, J. Appl. Mech. 68 (1) (2001) 34–41.
[4] A. F. Vakakis, Inducing passive nonlinear energy sinks in vibrating systems, J. Vib. Acoust. 123 (3) (2001) 324–332.
[5] G. Kerschen, A. F. Vakakis, Y. S. Lee, D. M. McFarland, J. J. Kowtko, L. A. Bergman, Energy transfers in a system of two coupled oscillators with essential nonlinearity: 1: 1 resonance manifold and transient bridging orbits, Nonlinear Dynamics 42 (3) (2005) 283–303.
[6] G. Kerschen, Y. S. Lee, A. F. Vakakis, D. M. McFarland, L. A. Bergman, Irreversible passive energy transfer in coupled oscillators with essential nonlinearity, SIAM Journal on Applied Mathematics 66 (2) (2005) 648–679.
[7] Y. S. Lee, G. Kerschen, A. F. Vakakis, P. Panagopoulos, L. Bergman, D. M. McFarland, Complicated dynamics of a linear oscillator with a light, essentially nonlinear attachment, Physica D: Nonlinear Phenomena 204 (1-2) (2005) 41–69.
[8] A. F. Vakakis, O. V. Gendelman, L. A. Bergman, D. M. McFarland, G. Kerschen, Y. S. Lee, Nonlinear targeted energy transfer in mechanical and structural systems, Vol. 156, Springer Science & Business Media, 2008.
[9] A. F. Vakakis, L. Manevitch, O. Gendelman, L. Bergman, Dynamics of linear discrete systems connected to local, essentially non-linear attachments, Journal of Sound and Vibration 264 (3) (2003) 559–577.
[10] K. Dekemele, R. De Keyser, M. Loccufier, Performance measures for targeted energy transfer and resonance capture cascading in nonlinear energy sinks, Nonlinear Dynamics 93 (2) (2018) 259–284.
[11] G. Habib, F. Romeo, Tracking modal interactions in nonlinear energy sink dynamics via high-dimensional invariant manifold, Nonlinear Dynamics (2020) 1–22.

[12] X. Kong, H. Li, C. Wu, Dynamics of 1-dof and 2-dof energy sink with geometrically nonlinear damping: application to vibration suppression, Nonlinear Dynamics 91 (1) (2018) 733–754.
[13] S. Charlemagne, C.-H. Lamarque, A. T. Savadkoohi, Vibratory control of a linear system by addition of a chain of nonlinear oscillators, Acta Mechanica 228 (9) (2017) 3111–3133.
[14] N. Benarous, O. V. Gendelman, Nonlinear energy sink with combined nonlinearities: Enhanced mitigation of vibrations and amplitude locking phenomenon, Proceedings of the Institution of Mechanical Engineers, Part C: Journal of Mechanical Engineering Science 230 (1) (2016) 21–33.
[15] T. Yang, S. Hou, Z.-H. Qin, Q. Ding, L.-Q. Chen, A dynamic reconfigurable nonlinear energy sink, Journal of Sound and Vibration (2020) 115629.
[16] G. Habib, F. Romeo, The tuned bistable nonlinear energy sink, Nonlinear Dynamics 89 (1) (2017) 179–196. doi:10.1007/s11071-017-3444-y.
[17] K. Dekemele, P. Van Torre, M. Loccufier, Performance and tuning of a chaotic bi-stable nes to mitigate transient vibrations, Nonlinear Dynamics 98 (3) (2019) 1831–1851.
[18] D. Lin, D. Oguamanam, Targeted energy transfer efficiency in a low-dimensional mechanical system with an essentially nonlinear attachment, Nonlinear Dynamics 82 (1-2) (2015) 971–986.
[19] J. E. Chen, M. Sun, W. H. Hu, J. H. Zhang, Z. C. Wei, Performance of non-smooth nonlinear energy sink with descending stiffness, Nonlinear Dynamics (2020) 1–13.
[20] D. M. McFarland, L. A. Bergman, A. F. Vakakis, Experimental study of non-linear energy pumping occurring at a single fast frequency, International journal of non-linear mechanics 40 (6) (2005) 891–899.
[21] S. L. Feudo, C. Touzé, J. Boisson, G. Cumunel, Nonlinear magnetic vibration absorber for passive control of a multi–storey structure, Journal of Sound and Vibration 438 (2019) 33–53.
[22] O. Gendelman, G. Sigalov, L. Manevitch, M. Mane, A. Vakakis, L. Bergman, Dynamics of an eccentric rotational nonlinear energy sink, Journal of applied mechanics 79 (1).
[23] G. Sigalov, O. Gendelman, M. Al-Shudeifat, L. Manevitch, A. Vakakis, L. Bergman, Resonance captures and targeted energy transfers in an inertially-coupled rotational nonlinear energy sink, Nonlinear dynamics 69 (4) (2012) 1693–1704.
[24] N. E. Wierschem, M. A. AL-Shudeifat, B. F. Spencer, A. F. Vakakis, L. A. Bergman, Experimental investigation of a rotational nonlinear energy sink for shock mitigation, in: ASME 2014 International Design Engineering Technical Conferences and Computers and Information in Engineering Conference, American Society of Mechanical Engineers Digital Collection, 2014.
[25] M. Farid, O. V. Gendelman, Tuned pendulum as nonlinear energy sink for broad energy range, Journal of Vibration and Control 23 (3) (2017) 373–388.
[26] M. A. AL-Shudeifat, N. E. Wierschem, L. A. Bergman, A. F. Vakakis, Numerical and experimental investigations of a rotating nonlinear energy sink, Meccanica 52 (4) (2017) 763–779.
[27] A. S. Saeed, M. A. AL-Shudeifat, A. F. Vakakis, Rotary-oscillatory nonlinear energy sink of robust performance, International Journal of Non-Linear Mechanics 117 (2019) 103249.
[28] A. Blanchard, L. A. Bergman, A. F. Vakakis, Vortex-induced vibration of a linearly sprung cylinder with an internal rotational nonlinear energy sink in turbulent flow, Nonlinear Dynamics 99 (1) (2020) 593–609.
[29] K. Dekemele, P. Van Torre, M. Loccufier, Design, construction and experimental performance of a nonlinear energy sink in mitigating multi-modal vibrations, Journal of Sound and Vibration 473 (2020) 115243.
[30] D. Zou, G. Liu, Z. Rao, T. Tan, W. Zhang, W.-H. Liao, A device capable of customizing nonlinear forces for vibration energy harvesting, vibration isolation, and nonlinear energy

sink, Mechanical Systems and Signal Processing 147 107101.
[31] J. Lee, T. Detroux, G. Kerschen, Enforcing a force–displacement curve of a nonlinear structure using topology optimization with slope constraints, Applied Sciences 10 (8) (2020) 2676.
[32] B. Vaurigaud, A. T. Savadkoohi, C.-H. Lamarque, Targeted energy transfer with parallel nonlinear energy sinks. part i: Design theory and numerical results, Nonlinear dynamics 66 (4) (2011) 763–780.
[33] O. V. Gendelman, Targeted energy transfer in systems with non-polynomial nonlinearity, Journal of Sound and Vibration 315 (3) (2008) 732–745.
[34] A. T. Savadkoohi, C.-H. Lamarque, Z. Dimitrijevic, Vibratory energy exchange between a linear and a nonsmooth system in the presence of the gravity, Nonlinear Dynamics 70 (2) (2012) 1473–1483.
[35] O. Gendelman, Y. Starosvetsky, M. Feldman, Attractors of harmonically forced linear oscillator with attached nonlinear energy sink i: description of response regimes, Nonlinear Dynamics 51 (1) (2008) 31–46.
[36] G. Habib, F. Kádár, B. Papp, Impulsive vibration mitigation through a nonlinear tuned vibration absorber, Nonlinear Dynamics 98 (3) (2019) 2115–2130.
[37] L. Dell'Elce, E. Gourc, G. Kerschen, A robust equal-peak method for uncertain mechanical systems, Journal of Sound and Vibration 414 (2018) 97–109.
[38] J. C. Lagarias, J. A. Reeds, M. H. Wright, P. E. Wright, Convergence properties of the nelder–mead simplex method in low dimensions, SIAM Journal on optimization 9 (1) (1998) 112–147.

Appendix A. Realization

A conventional NES was realized in [29] and was based on the mechanism in Figure A.1a. A mass, constrained in the x-direction, features axial springs on rollers that, under a static force F_x, are compressed according to a machined or 3D-printed force profile that has a function $f(x)$. The force F_x and the displacement of the absorber x is related by the force profile $f(x)$:

$$F_x = k_l f(x) \frac{df(x)}{dx} \tag{A.1}$$

To achieve a cubic nonlinear stiffness, this force profiled should be a parabola. The experimental realization is shown in Figure A.1b. To achieve any tailor-made stiffness characteristic, the force profile should equal the square of the elastic energy of the spring:

$$f(x) = \sqrt{\frac{1}{k_l} \int_0^x F(x) + C} \tag{A.2}$$

Where the term $\int_0^x F(x)$ is the potential energy of the desired characteristic. This result was also presented in [30]. The force profile for the periodically extended cubic stiffness NES is shown in Figure A.1c. However, the sharp kinks in the force profile might cause issues in the realization and the rollers attached to the axial springs. A proposal to smooth out the discontinuities in the spring characteristic is found in Appendix D, which will also smooth out the kinks in the force profile.

Appendix B. First harmonic of periodically-extended NES

The integral (9) is solved here if the stiffness is (2). Under steady state, $B = be^{j\beta}$, $z = \frac{Be^{j\tau} - \bar{B}e^{-j\tau}}{2j} = b\sin(\tau + \beta)$. Solving the integral depends on the amplitude of vibration b.

Appendix B.1. $b < d$

For $b < d$, only the part where $F(z) = z^3$ has to be considered:

$$\begin{aligned} f1 &= \frac{e^{j\beta}}{2\pi} \int_0^{2\pi} (b\sin(\tau_b))^3 e^{-j\tau_b} d\tau_b \\ &= -j\frac{3b^3 e^{j\beta}}{8} = -j\frac{B}{2}\frac{3b^2}{4} \end{aligned} \tag{B.1}$$

where $\tau_b = \tau + \beta$. Here $G(b) = \frac{3b^2}{4}$, which is the same for the conventional NES.

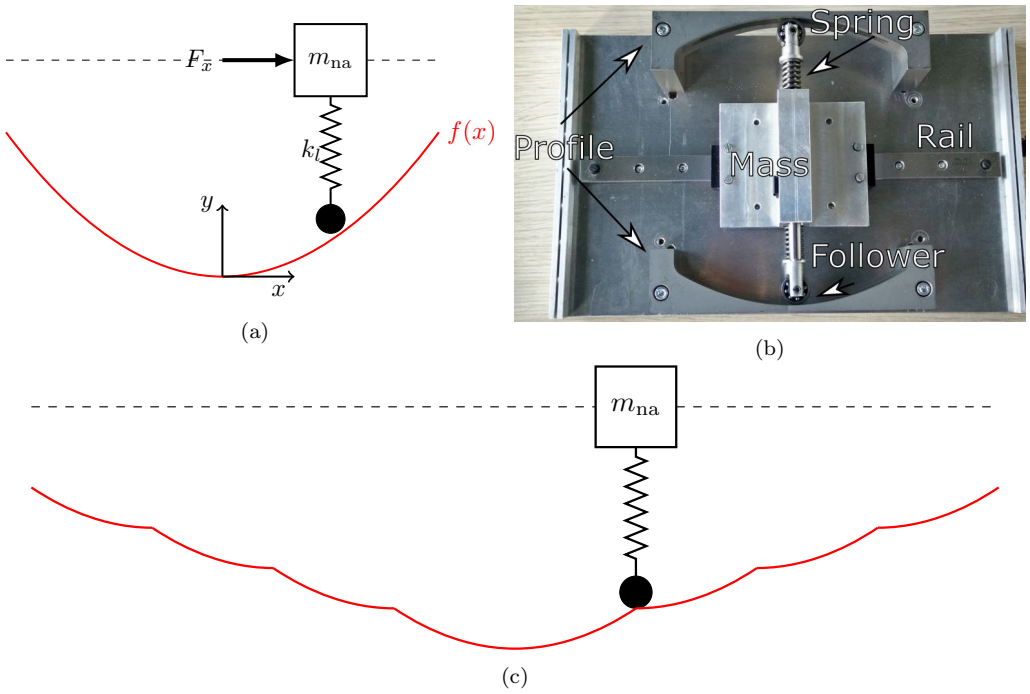

Figure A.1: The concept of the conventional NES realization (a) and realization (b) in [29], and periodically extended to create the novel NES presented in this paper, (b).

Appendix B.2. $d < b < 2d$

For this amplitude, the first periodic extension in both negative and positive direction have to be included in the integral:

$$\begin{aligned} f1 = \frac{e^{j\beta}}{2\pi}\Bigg(& \int_0^{\text{asin}(\frac{d}{b})} (b\sin(\tau_b))^3 e^{-j\tau_b} d\tau_b + \int_{\text{asin}(\frac{d}{b})}^{\pi-\text{asin}(\frac{d}{b})} (b\sin(\tau_b) - d)^3 e^{-j\tau_b} d\tau_b \\ & + \int_{\pi-\text{asin}(\frac{d}{b})}^{\pi+\text{asin}(\frac{d}{b})} (b\sin(\tau_b))^3 e^{-j\tau_b} d\tau_b + \int_{\pi+\text{asin}(\frac{d}{b})}^{2\pi-\text{asin}(\frac{d}{b})} (b\sin(\tau_b) + d)^3 e^{-j\tau_b} d\tau_b \\ & + \int_{2\pi-\text{asin}(\frac{d}{b})}^{2\pi} (b\sin(\tau_b))^3 e^{-j\tau_b} d\tau_b \Bigg) \\ = & \frac{e^{i\beta}}{2\pi}\Bigg(- 8b^2\sqrt{\frac{b^2-d^2}{b^2}}d - 2d^3\sqrt{\frac{b^2-d^2}{b^2}} - 6d^2 b\text{asin}(\frac{d}{b}) + \frac{3\pi b^3}{4} + 3d^2 b\pi \Bigg) \end{aligned} \tag{B.2}$$

Appendix B.3. $nd < b < (n+1)d$

For an amplitude $nd < b < (n+1)d$, the NES reaches the periodic extension up to and including $(z-nd)^3$ for positive displacements and $(z+nd)^3$ for negative. The integral is split into pieces, $f1 = \sum_{i=0}^{n} f1i$ where $f1i$ is the contribution for when $|z| = |b\sin(\tau_b + \beta)| < (i+1)d$. For $i = 0$:

$$\begin{aligned} f10 = & \frac{e^{j\beta}}{2\pi}\Bigg(\int_0^{\text{asin}(\frac{d}{b})} (b\sin(\tau_b))^3 e^{-j\tau_b} d\tau_b + \int_{\pi-\text{asin}(\frac{d}{b})}^{\pi+\text{asin}(\frac{d}{b})} (b\sin(\tau_b))^3 e^{-j\tau_b} d\tau_b \\ & + \int_{2\pi-\text{asin}(\frac{d}{b})}^{2\pi} (b\sin(\tau_b))^3 e^{-j\tau_b} d\tau_b \Bigg) \\ = & -j\frac{e^{j\beta}}{2\pi}\Bigg(- d^3\sqrt{\frac{b^2-d^2}{b^2}} + \frac{3}{2}b^3\text{asin}(\frac{d}{b}) - \frac{3}{2}b^2\sqrt{\frac{b^2-d^2}{b^2}}d \Bigg) \end{aligned} \tag{B.3}$$

where $\tau_b = \tau + \beta$

For $0 < i < n$

$$f1i = \frac{e^{j\beta}}{2\pi}\left(\int_{\text{asin}(\frac{id}{b})}^{\text{asin}(\frac{(i+1)d}{b})} (b\sin(\tau_b) - id))^3 e^{-j\tau_b} d\tau_b + \int_{\pi-\text{asin}(\frac{(i+1)d}{b})}^{\pi-\text{asin}(\frac{id}{b})} (b\sin(\tau_b) - id))^3 e^{-j\tau_b} d\tau_b \right.$$
$$\left. + \int_{\pi+\text{asin}(\frac{id}{b})}^{\pi+\text{asin}(\frac{(i+1)d}{b})} (b\sin(\tau_b) + id))^3 e^{-j\tau_b} d\tau_b \int_{2\pi-\text{asin}(\frac{(i+1)d}{b})}^{2\pi-\text{asin}(\frac{id}{b})} (b\sin(\tau_b) + id))^3 e^{-j\tau_b} d\tau_b \right)$$
$$= -j\frac{e^{j\beta}}{2\pi}\left(\frac{13}{2}\left(\frac{2(i-1)(i^2+1)d^2}{13} + b^2(i - \frac{3}{13}) \right) d\sqrt{\frac{b^2-(i+1)^2d^2}{b^2}} \right.$$
$$\left. + \frac{1}{2}(-2d^3i^3 - 13b^2di)\sqrt{\frac{-d^2i^2+b^2}{b^2}} - \frac{3}{2}b^2(4d^2i^2+b^2)\left(\text{asin}\left(\frac{id}{b}\right) - \text{asin}\left(\frac{(i+1)d}{b}\right)\right)\right) \tag{B.4}$$

and finally for $i = n$

$$f1n = \frac{e^{j\beta}}{2\pi}\left(\int_{\text{asin}(\frac{nd}{b})}^{\pi-\text{asin}(\frac{nd}{b})} (b\sin(\tau_b) - nd)^3 e^{-j\tau_b} d\tau_b + \int_{\pi+\text{asin}(\frac{nd}{b})}^{2\pi-\text{asin}(\frac{nd}{b})} (b\sin(\tau_b) + nd)^3 e^{-j\tau_b} d\tau_b \right)$$
$$= -j\frac{e^{i\beta}}{2\pi}\left(\frac{1}{4}(-4d^3n^3 - 26b^2n)\sqrt{\frac{-d^2n^2+b^2}{b^2}} + \frac{3}{4}b(4d^2n^2+b^2)\left(\pi - 2\text{asin}\left(\frac{nd}{b}\right)\right)\right) \tag{B.5}$$

Appendix C. Stability

The derivatives to calculate are:

$$\begin{aligned} \frac{\partial(B\cdot G(B,\bar{B}))}{\partial B} &= G(B,\bar{B}) + B\frac{\partial(G(B,\bar{B}))}{\partial B} \\ \frac{\partial(B\cdot G(B,\bar{B}))}{\partial \bar{B}} &= B\frac{\partial(G(B,\bar{B}))}{\partial \bar{B}} \end{aligned} \tag{C.1}$$

Appendix C.1. $b < d$

From (B.1) where $b = |B|$:

$$\begin{aligned} G(B,\bar{B}) &= \frac{3}{4}|B|^2 = \frac{3}{4}B\bar{B} \\ \frac{\partial(G(B,\bar{B}))}{\partial B} &= \frac{3}{4}\bar{B} \\ \frac{\partial(G(B,\bar{B}))}{\partial \bar{B}} &= \frac{3}{4}B \end{aligned} \tag{C.2}$$

Appendix C.2. $nd < b < (n+1)d$

When the NES vibrates in the periodic extensions, the integral is split up in parts as in (B.3) to (B.5). From these integrals $G(B,\bar{B}) = B\sum_{i=0}^{n} G_i(B,\bar{B})$, where the derivatives are then:

$$\begin{aligned} \frac{\partial(G(B,\bar{B}))}{\partial B} &= \frac{\partial(\sum_{i=0}^{n} G_i(B,\bar{B}))}{\partial B} \\ \frac{\partial(G(B,\bar{B}))}{\partial \bar{B}} &= \frac{\partial(\sum_{i=0}^{n} G_i(B,\bar{B}))}{\partial \bar{B}} \end{aligned} \tag{C.3}$$

where $G_0(B,\bar{B})$

$$G_0(B,\bar{B}) = -\frac{1}{\pi}\left(-\frac{d^3}{|B|^2}\sqrt{|B|^2-d^2} + \frac{3}{2}|B|^2 \mathrm{asin}\left(\frac{d}{|B|}\right) - \frac{3}{2}\sqrt{|B|^2-d^2}d\right)$$

$$\frac{\partial(G_0(B,\bar{B}))}{\partial B} = -\frac{1}{\pi}\left(-\frac{3d\bar{B}}{4\sqrt{|B|^2-d^2}} + \frac{d^3\sqrt{|B|^2-d^2}}{\bar{B}\,B^2} - \frac{d^3}{2B\sqrt{|B|^2-d^2}} + \frac{3\bar{B}\mathrm{asin}\left(\frac{d}{|B|}\right)}{2} - \frac{3d\,\bar{B}^2 B}{4|B|^3\sqrt{-\frac{d^2}{|B|^2}+1}}\right)$$

$$\frac{\partial(G_0(B,\bar{B}))}{\partial \bar{B}} = \overline{\frac{\partial(G_0(B,\bar{B}))}{\partial B}}$$

and $G_i(B,\bar{B})$ for $1 < i < n$:

$$G_i(B,\bar{B}) = -\frac{1}{\pi}\left(\frac{13d\left(\frac{2(i-1)\left(i^2+1\right)d^2}{13|B|^2}+i-\frac{3}{13}\right)\sqrt{|B|^2-(i+1)^2d^2}}{2}\right.$$
$$\left.+\frac{\left(-\frac{2i^3d^3}{|B|^2}-13id\right)\sqrt{-i^2d^2+|B|^2}}{2}-\frac{3\left(4i^2d^2+|B|^2\right)\left(\operatorname{asin}\left(\frac{id}{|B|}\right)-\operatorname{asin}\left(\frac{(i+1)d}{|B|}\right)\right)}{2}\right)$$

$$\frac{\partial(G_i(B,\bar{B}))}{\partial B} = -\frac{d^3\left(i-1\right)\left(i^2+1\right)\sqrt{|B|^2-(i+1)^2d^2}}{\bar{B}\,B^2}+\frac{13d\left(\frac{2(i-1)\left(i^2+1\right)d^2}{13|B|^2}+i-\frac{3}{13}\right)\bar{B}}{4\sqrt{|B|^2-(i+1)^2d^2}}$$
$$+\frac{i^3d^3\sqrt{-i^2d^2+|B|^2}}{\sqrt{B}\,B^2}+\frac{\left(-\frac{2i^3d^3}{|B|^2}-13id\right)\bar{B}}{4\sqrt{-i^2d^2+|B|^2}}-\frac{3\bar{B}\left(\operatorname{asin}\left(\frac{id}{|B|}\right)-\operatorname{asin}\left(\frac{(i+1)d}{|B|}\right)\right)}{2}$$
$$-\frac{3\left(4i^2d^2+|B|^2\right)\left(-\frac{id\bar{B}}{2|B|^3\sqrt{-\frac{d^2i^2}{|B|^2}+1}}+\frac{(i+1)d\bar{B}}{2|B|^2\sqrt{-\frac{(i+1)^2d^2}{|B|^2}+1}}\right)}{2}$$

$$\frac{\partial(G_i(B,\bar{B}))}{\partial\bar{B}} = \overline{\frac{\partial(G_i(B,\bar{B}))}{\partial B}}$$

and finally $G_n(B,\bar{B})$:

$$G_n(B,\bar{B}) = -\frac{1}{\pi}\left(\frac{\left(\frac{-4d^3n^3}{|B|^2}-26dn\right)\sqrt{-d^2n^2+|B|^2}}{4}\right.$$
$$\left.+\frac{3\left(4d^2n^2+|B|^2\right)\left(\pi-2\operatorname{asin}\left(\frac{nd}{|B|}\right)\right)}{4}\right)$$

$$\frac{\partial(G_n(B,\bar{B}))}{\partial B} = -\frac{1}{\pi}\left(\frac{d^3n^3\sqrt{-d^2n^2+|B|^2}}{\bar{B}\,B^2}+\frac{\left(-\frac{4d^3n^3}{|B|^2}-26nd\right)\bar{B}}{8\sqrt{-d^2n^2+|B|^2}}\right.$$
$$\left.+\frac{3\bar{B}\left(\pi-2\operatorname{asin}\left(\frac{nd}{|B|}\right)\right)}{4}+\frac{3\left(4d^2n^2+|B|^2\right)nd\bar{B}}{4|B|^3\sqrt{-\frac{n^2d^2}{|B|^2}+1}}\right)$$

$$\frac{\partial(G_n(B,\bar{B}))}{\partial\bar{B}} = \overline{\frac{\partial(G_n(B,\bar{B}))}{\partial B}}$$

Appendix D. Smoothed NES restoring force function

Depending on the mechanism utilized for the practical realization of a periodically extended NES, the discontinuities of the restoring force function might cause technological challenges. In this section, we verify that eliminating those discontinuities does not compromise the performance of the absorber. The restoring force function $F(z)$ has discontinuities for $z = \pm id$, for $i \in \mathbb{N}^+$. In order to make $F(z)$ differentiable, for

$$id - s/2 < z < id + s/2, \tag{D.1}$$

we substitute $F(z)$ with the third order polynomial function

$$\tilde{F}(\tilde{z}) = a_0 + a_1\tilde{z} + a_2\tilde{z}^2 + a_3\tilde{z}^3, \tag{D.2}$$

where $0 < s < d/2$ is an arbitrarily small positive real number. The coefficients a_0, a_1, a_2 and a_3 are chosen such that $\tilde{F}(\tilde{z})$ has the same value and the same first derivative of $F(z)$ for $z = id - s/2$ and $z = id + s/2$. For $z > 0$, the new variable $\tilde{z}$ is defined as

$$\tilde{z} = z - \left\lfloor \frac{x + s/2}{d} \right\rfloor + s/2, \tag{D.3}$$

besides,

$$\begin{aligned} a_0 &= (d - s/2)^3 \\ a_1 &= 3\,(d - s/2)^2 \\ a_2 &= -\frac{3\left(4d^3 + 2d^2 s - 5ds^2 + 2s^3\right)}{4s^2} \\ a_3 &= \frac{2d^3}{s^3} - \frac{3d}{2s} + 1. \end{aligned} \tag{D.4}$$

Eventually, Eq. (2) is substituted by

$$F(z) = \begin{cases} F_1(z) & z \geq 0 \\ F_2(z) & z < 0, \end{cases} \tag{D.5}$$

where

$$F_1(z) = \begin{cases} \left(z - \left\lfloor \frac{z}{d} \right\rfloor d\right)^3 & \frac{s}{2} < z - \left\lfloor \frac{z}{d} \right\rfloor d < d - \frac{s}{2} \quad \text{or} \quad z < \frac{d}{2} \\ a_0 + a_1\tilde{z} + a_2\tilde{z}^2 + a_3\tilde{z}^3 & z > \frac{d}{2} \text{ and } \left(z - \left\lfloor \frac{z}{d} \right\rfloor d < \frac{s}{2} \text{ or } z - \left\lfloor \frac{z}{d} \right\rfloor d > d - \frac{s}{2}\right) \end{cases} \tag{D.6}$$

and $F_2(z) = -F_1(-z)$. Figure D.2a provides a comparison between the original discontinuous restoring force and the continuous one. In the figure $d = 3$, while

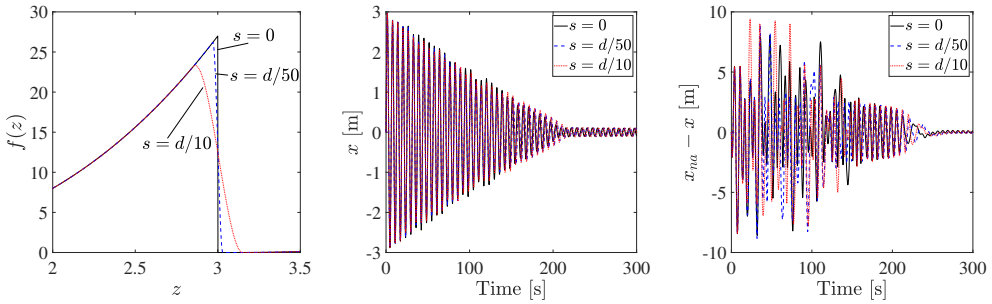

(a) (b) (c)

Figure D.2: a) Restoring force function compared to its continuous counterpart for $s = d/50$ and $s = d/10$. (b) Comparison of displacements of the primary system in time, for the same parameter values, except the smoothing coefficient s. (c) Relative displacement of the periodically extended NES.

$s = d/50$ and $s = d/10$. $s = 0$ corresponds to the discontinuous case. We performed time integration of the mechanical system, using the same parameter values of Fig. 5, for different values of s ($s = d/50$ and $s = d/10$). The resulting time series are provided in Figs. D.2b and D.2c. We notice that, although the NES relative displacement is quite different in the three cases, the envelope of the vibrations in the primary system is practically unchanged, which suggests that eliminating the discontinuity of the NES restoring force function does not compromises its performance.